ACS NANO

www.acsnano.org

ARTICLE

# Precision Synthesis of Bimetallic Nanoparticles via Nanofluidics in Nanopipets

Heekwon Lee, Kevin C. Matthews, Xun Zhan, Jamie H. Warner, and Hang Ren*

Cite This: *ACS Nano* 2023, 17, 22499–22507

Read Online

ACCESS | Metrics & More | Article Recommendations | Supporting Information

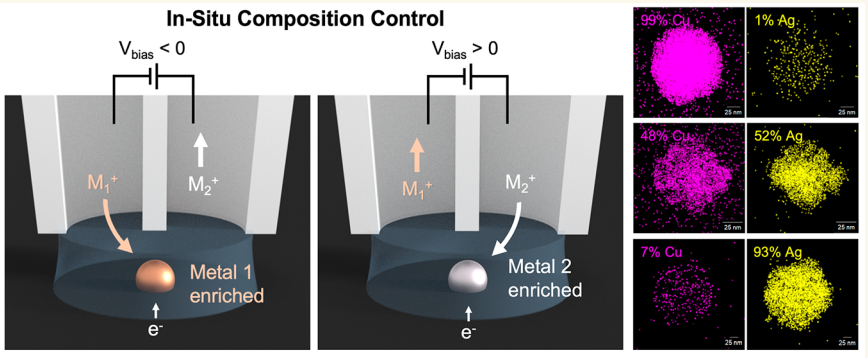


**ABSTRACT:** **Bimetallic nanoparticles often show properties superior to their single-component counterparts. However, the large parameter space, including size, structure, composition, and spatial arrangement, impedes the discovery of the best nanoparticles for a given application. High-throughput methods that can control the composition and spatial arrangement of the nanoparticles are desirable for accelerated materials discovery. Herein, we report a methodology for synthesizing bimetallic alloy nanoparticle arrays with precise control over their composition and spatial arrangement. A dual-channel nanopipet is used, and nanofluidic control in the nanopipet further enables precise tuning of the electrodeposition rate of each element, which determines the final composition of the nanoparticle. The composition control is validated by finite element simulation as well as electrochemical and elemental analyses. The scope of the particles demonstrated includes Cu−Ag, Cu−Pt, Au−Pt, Cu−Pb, and Co−Ni. We further demonstrate surface patterning using Cu−Ag alloys with precise control of the location and composition of each pixel. Additionally, combining the nanoparticle alloy synthesis method with scanning electrochemical cell microscopy (SECCM) allows for fast screening of electrocatalysts. The method is generally applicable for synthesizing metal nanoparticles that can be electrodeposited, which is important toward developing automated synthesis and screening systems for accelerated material discovery in electrocatalysis.**

**KEYWORDS:** *automated synthesis, nanoparticle alloys, electrodeposition, scanning electrochemical cell microscopy, nanopipet*

Here, we report a method for the serial synthesis of alloy nanoparticle arrays with controlled metallic composition and spatial arrangement. Metallic nanoparticles have physical and chemical properties that enable their wide application in many fields, including catalysis, optics, electronics, and biomedicine.[1−3] Precision nanoparticle synthesis to control the size, shape, facet, and ligand has provided a fundamental understanding of the structure−function relationship of nanoparticles as electrocatalysts for reactions like hydrogen evolution reaction, oxygen reduction reaction, and $CO_2$ reduction reaction.[4−6] However, the size, structure, and spatial arrangement present significant challenges in finding the optimal nanoparticles for specific reactions due to the exponential increase in parameter space.[7] Metal nanoparticle alloys, which can assume better electrocatalytic activity than nanoparticles of a single element, introduce further complexity in the parameter space in terms of the atomic composition.[8,9] Additionally, even with the same atomic composition, the variation in the atomic arrangement can lead to structures from intermetallic compounds to alloys and heterogeneously structured nanoparticles, which have different properties.[6,10] Furthermore, although spatially arranging nano-

Received: July 2, 2023
Revised: October 29, 2023
Accepted: October 31, 2023
Published: November 6, 2023

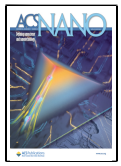




https://doi.org/10.1021/acsnano.3c06011
*ACS Nano* 2023, 17, 22499−22507

particles to enable tandem catalysis is promising in controlling the efficiency and selectivity in electrocatalytic reactions,[11] conventional methods of nanoparticle synthesis offer no spatial control of the particles on the electrode. Developing a high-throughput synthesis method that allows continuous compositional control and sufficient spatial control of the particles is highly desirable.

High-throughput synthesis is an important step in accelerated materials discovery for electrocatalysis.[7,12,13] To this end, Mallouk and co-workers have reported alloy catalyst arrays prepared by aqueous metal precursor solutions with a liquid handler followed by hydrazine reduction.[14] Mirkin and co-workers have developed a dip-pen nanolithography (DPN) approach to synthesize multielemental alloy nanoparticles using premade metal precursor ink.[10,15−17] While this method demonstrates an effective approach for synthesizing alloy nanoparticle libraries, the spatial control of nanoparticles is predetermined by the master substrate created through lithography. Also, the precursor solutions need to be prepared with a specific mole fraction before initiating the synthesis, which limits the on-demand control of the composition of the alloy at specific locations. Furthermore, combinatorial sputtering[18] and optical ablation[19] have been demonstrated to yield alloy nanoparticles. However, high-degree control over the spatial positioning of nanoparticles requires multistep methods such as lithographic techniques or manipulation of presynthesized nanoparticles by sharp probes.[20] Also, the use of ligands to stabilize the nanoparticles adds another layer of complexity, which can often block the active sites of the electrocatalysts.[21,22]

Electrochemistry is an effective method to challenge the intricacies involved in alloy nanoparticle synthesis without the need for a ligand.[9,23,24] In electrodeposition, the driving force, i.e., the electrode potential, can be readily controlled in real time, while the rate of electrodeposition can be monitored as the current. This allows for quantitative control of the nucleation and growth processes during nanoparticle synthesis. Moreover, direct electrodeposition on the electrode surfaces offers better attachment. However, several challenges exist in the electrodeposition of nanoparticles. First, the distribution of the nucleation sites and the stochastic nature of nucleation make the control of the spatial arrangement of nanoparticle challenging.[25] Second, the throughput of electrodeposition to synthesize nanoparticles using conventional methods, such as bulk solution synthesis, is intrinsically low.

Scanning electrochemical cell microscopy (SECCM) has emerged as a promising method for electrodeposition of metallic nanoparticles with high spatial resolution and precise control over their size and shape.[26−28] Herein, we develop a dual-channel SECCM method to synthesize bimetallic nanoparticles with control of the elemental composition and the location of the nanoparticles. Each barrel of the nanopipet is filled with different metal precursors (e.g., Cu and Ag) to be reduced on the electrode. The composition of the nanoparticles is controlled by changing the solution composition in the SECCM droplet cell in situ via migration and electroosmotic flow.[29] Additionally, the catalytic activity of the spatially and compositionally controlled bimetallic nanoparticles can be further screened by single-channel SECCM.[30−32] The developed platform will enable opportunities for the accelerated discovery of nanomaterials as electrocatalysts through high-throughput electrocatalyst synthesis and screening.

## RESULTS AND DISCUSSION

SECCM is used for depositing bimetallic particles because it can confine the deposition locally within the nanodroplet and allow control of the location of particles. As illustrated in Scheme 1, a dual-barrel glass pipet filled with solutions

**Scheme 1. Schematic Illustration of On-Demand Deposition of Cu−Ag Nanoparticle Array by SECCM[a]**

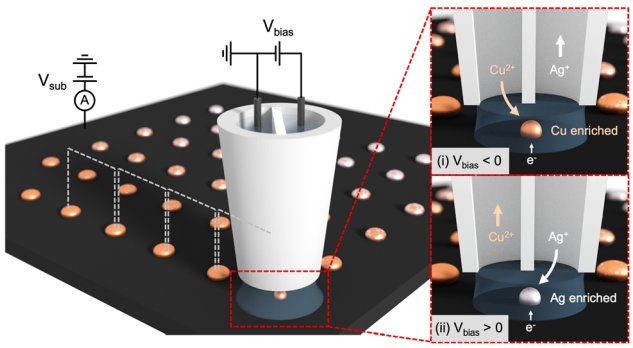


[a]Control of mole fractions from Cu-rich to Ag-rich Cu−Ag nanoparticles by varying the bias potential between two barrels ($V_{bias}$) during electrodeposition. The bias controls the electroosmotic flow and migration of metal precursors in an attoliter cell on the substrate.

containing metal precursors, e.g., $Ag^+$ or $Cu^{2+}$, is used as the probe. A typical dual-barrel pipet has an ~340 nm radius in the opening, as shown in Figure S1. The meniscus at the end of the pipet is controlled to contact the substrate, e.g., glassy carbon (GC), and a sudden flow of current due to the completion of the circuit serves as feedback. The contact area between the droplet and the substrate defines a local electroactive area for electrodeposition that occurs when a potential ($V_{sub}$) is applied between the substrate and the quasi-reference counter electrode (QRCE) in the bulk portion of the pipet. After deposition at one location, the pipet can be retracted and moved to a new location for a new deposition. The process can be repeated at hundreds or thousands of locations, allowing surface patterning and serial synthesis of nanoparticle libraries for catalyst screening.

Alloy particles can be synthesized when multiple metal precursors are present in the solution. In situ composition control is achieved by tuning the solution composition in the droplet using a dual-barrel pipet SECCM, with each barrel containing one type of precursor. The concept is illustrated in Scheme 1 using a Cu−Ag bimetallic particle as an example. The left barrel is filled with Cu precursor (2 mM $Cu^{2+}$ in 2 mM $HClO_4$), and the right barrel is filled with Ag precursor (2 mM $Ag^+$ in 2 mM $HClO_4$). A potential bias between the two QRCEs in the two barrels ($V_{bias}$, right vs left) controls the relative amount of $Cu^{2+}$ and $Ag^+$ in the droplet via migration and electroosmotic flow. When 0 V bias is applied, $Cu^{2+}$ and $Ag^+$ are expected to mix relatively evenly in the droplet by diffusion. When $V_{bias}$ < 0 V is applied, i.e., the $Ag^+$-containing barrel having lower potential, cations will migrate from the $Cu^{2+}$ barrel (left) to the $Ag^+$ barrel (right), as shown in scenario (i) in Scheme 1. As a result, $Cu^{2+}$ will move into the right barrel through the droplet, while $Ag^+$ will recede deep into the right barrel. The net result is enrichment of $Cu^{2+}$ and depletion of $Ag^+$ in the droplet cell. Electrodeposition under this condition is expected to produce particles enriched in Cu.


https://doi.org/10.1021/acsnano.3c06011
ACS Nano 2023, 17, 22499−22507

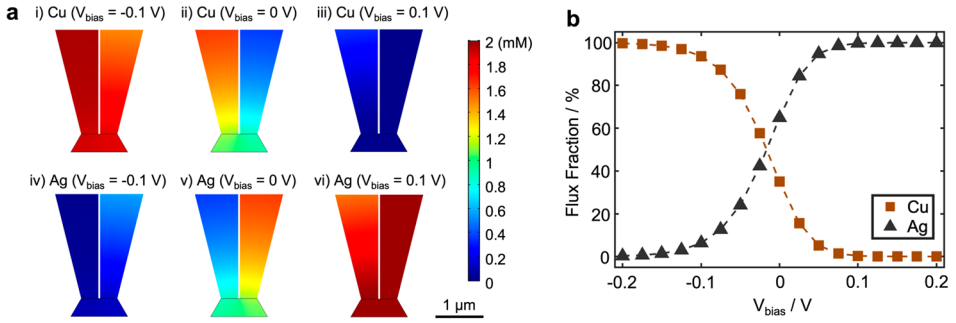


**Figure 1. Finite element simulation of electrochemical deposition of bimetals in a dual-barrel pipet. (a) Concentration profiles of $Cu^{2+}$ and $Ag^{+}$ when the bias potentials ($V_{bias}$) of −0.1, 0, and 0.1 V are applied without electrochemical metal reduction on the substrate (bottom). Only the portion near the tip of the pipet is shown. (b) Simulated flux fraction of $Cu^{2+}$ and $Ag^{+}$ at the substrate as a function of $V_{bias}$ when electrochemical metal reduction is operated at the mass-transport-limited rate on the substrate.**

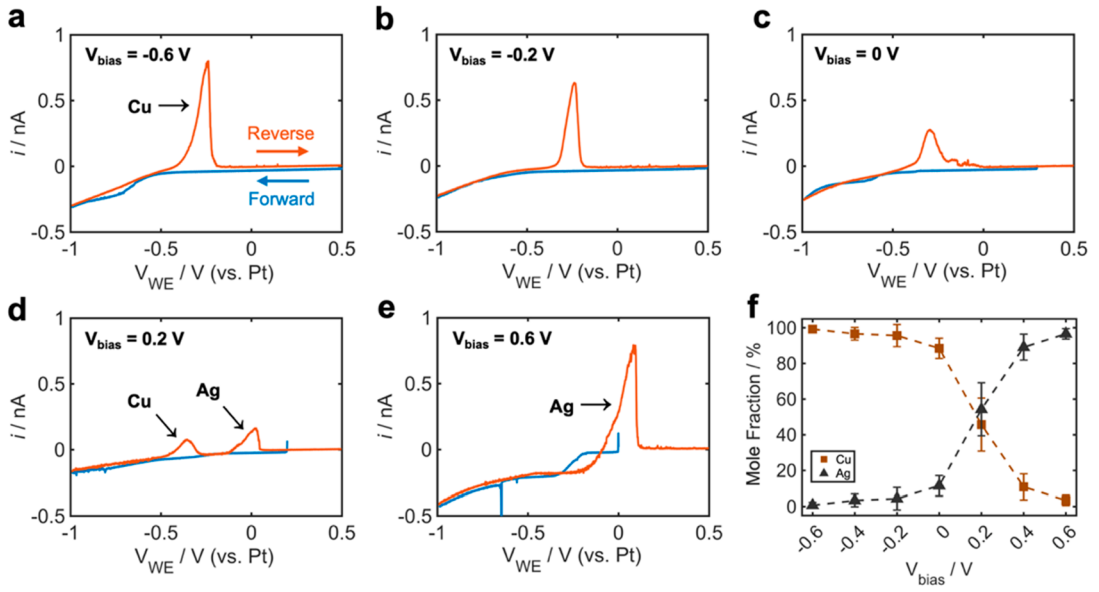


**Figure 2. Cyclic voltammograms for the deposition and stripping of Cu−Ag bimetallic particles in SECCM at different $V_{bias}$: (a) −0.6 V, (b) −0.2 V, (c) 0 V, (d) 0.2 V, and (e) 0.6 V. (f) Mole fraction of Cu and Ag in the bimetallic particle calculated from the charge in the anodic stripping peaks in the voltammograms. Error bars represent the standard deviation from $n$ = 5. One barrel contains 2 mM $Cu(ClO_4)_2$ and 2 mM $HClO_4$; the other contains 2 mM $AgClO_4$ and 2 mM $HClO_4$. Scan rate: 0.5 V/s.**

Similarly, when $V_{bias} > 0$ is applied, the droplet will be enriched with $Ag^{+}$, allowing the deposition of Ag-enriched nanoparticles. The extent of enrichment of Ag versus Cu can be continuously tuned by $V_{bias}$. Note that electroosmotic flow can also affect the flux of each ion, but its contribution is expected to be small in 2 mM $HClO_4$ because the quartz has a low surface charge density at this pH. Although the synthesis of bimetallic particles is the focus of this paper, the general principle can be extended for the synthesis of multielement particles, including high-entropy alloys, when multibarrel pipets are used.

The ability to control the solution composition of the droplet is quantitatively validated by finite element simulation to obtain the concentration profile and the ionic flux of metal precursors in a dual-barrel pipet. A 3D model is constructed in COMSOL Multiphysics, and the effects of diffusion, migration, and electroosmotic flow are evaluated by solving the Nernst−Planck equation assuming neutrality. More details about the simulation are described in Section S2 in the Supporting Information. Figure 1a shows the simulated concentration profiles of $Cu^{2+}$ and $Ag^{+}$ at different $V_{bias}$. No metal deposition is implemented at the substrate to better visualize the movement of ions. At $V_{bias}$ = −0.1 V (right barrel vs left), an enrichment of $Cu^{2+}$ and depletion of $Ag^{+}$ in the droplet and right barrel are observed due to cation migration from the left barrel to the right. Similarly, enrichment of $Ag^{+}$ and depletion of $Cu^{2+}$ in the droplet is observed at +0.1 V. To verify the flux of metal deposition under different $V_{bias}$, a similar simulation was performed except that metal precursors were electrodeposited (i.e., consumed) at the substrate at the mass-transport-limited rate. The concentration profiles under these conditions are shown in Figure S3. The resulting flux of $Ag^{+}$ and $Cu^{2+}$ as a function of $V_{bias}$ is shown in Figure 1b. As expected, the preferred deposition of Cu and Ag is observed at negative and positive $V_{bias}$, respectively. The flux of each species varies from ∼100% to ∼0% over a 200 mV range of $V_{bias}$.

Experimentally, we also used the Cu−Ag system as an example to validate the control of the nanoparticle



https://doi.org/10.1021/acsnano.3c06011
ACS Nano 2023, 17, 22499−22507

composition in electrodeposition. Cyclic voltammetry was performed, and the nucleation and growth of metal particles were induced in the negative-going scan, while the stripping peaks in the positive-going scans could be used to quantify the amount of each metal deposit by using Faraday's law of electrolysis. Cyclic voltammograms at different $V_{bias}$ are shown in Figure 2a–e. Note that the working electrode potential, $V_{WE}$, is approximated by $V_{sub} - 0.5V_{bias}$, where $V_{sub}$ is the potential applied on the substrate vs the ground.[29,33] At $V_{bias}$ = −0.6 V (Figure 2a), the scan starts at 0.5 V (vs Pt QRCE) in the negative direction, and the current begins to increase as $V_{WE}$ becomes more negative than −0.5 V, corresponding to the electrochemical reduction of $Cu^{2+}$ to metallic Cu. In the reverse scan, a single stripping peak is observed at $V_{WE} \approx -0.3$ V, corresponding to the anodic stripping of Cu deposited in the previous scan. At $V_{bias}$ = −0.2 V, a similar voltammetric behavior is observed, except that a smaller deposition current in the negative-going scan and a smaller stripping peak are observed, suggesting that less Cu is deposited. At $V_{bias}$ = 0 V, the anodic stripping peak is further decreased. This peak also becomes wider from the emergence of a second peak. When $V_{bias}$ is increased to 0.2 V (Figure 2d), two distinct anodic stripping peaks are observed, one at ∼−0.4 V and the other at ∼0 V, which are assigned to the anodic stripping of Cu and Ag, respectively (see Section S3 in the Supporting Information for the discussion about the assignment). The 0.4 V difference between the two peaks is close to the difference in $E^{\circ}$ for $Ag/Ag^{+}$ (0.799 V) and $Cu/Cu^{2+}$ (0.340 V). The small deviation (ca. 0.06 V) is attributed to the potential difference in the kinetics of the metal dissolution reactions. Additionally, the stabilization of Cu in the bimetallic particle would also lead to a more positive potential to strip Cu, narrowing the gap between the stripping peaks. When $V_{bias}$ is further increased to 0.6 V, the stripping peak corresponding to Cu is almost invisible, while the peak for Ag increases significantly (Figure 2e), suggesting that the deposit predominantly contains Cu. The mole fractions of Cu and Ag in the deposits are quantified from the stripping peaks at different $V_{bias}$, shown in Figure 2f. At negative bias, deposition is dominated by Cu (>90% by mole fraction), consistent with scenario (i) in Scheme 1. As $V_{bias}$ increases, the fraction of Cu decreases while the fraction of Ag increases, which agrees with our finite element simulation (Figure 1). At $V_{bias}$ > 0.4 V, the deposit is dominated by Ag, consistent with scenario (ii) in Scheme 1. The mole ratio reaches 1:1 at $V_{bias}$ of ∼0.2 V, not at 0 V. This is mainly because the two Pt QRCEs are in different solutions, and their potentials are expected to differ, as Pt itself is often not a good reference electrode. This is supported by the deposition of Cu–Ag using $Pd-H_2$ electrodes, which assume well-defined potential from the $H^{+}/H_2$ couple. As shown in Figure S8, a mole ratio of 1:1 for Cu:Ag is formed at a $V_{bias}$ of ∼−0.03 V. A junction potential created when mixing different solutions in the two barrels is also expected to contribute to the nonzero $V_{bias}$ as a secondary effect. Regardless, the variation of deposit composition as a function of $V_{bias}$ (Figure 2f) demonstrates the ability of this method to control the composition during the electrosynthesis of nanoparticles, which is the focus of this paper. The detailed fluidic control and potential distribution are systematically evaluated and reported in a separate study.

Control of the composition of metal deposits by $V_{bias}$ is further simplified by using a constant deposition potential instead of voltammetry, as shown in Section S5 in the Supporting Information and Figure S9. Annular dark field-scanning transmission electron microscopy (ADF-STEM) and energy-dispersive X-ray spectroscopy (EDS) images were used to verify the structure and composition of the particles deposited at the same $V_{WE}$ but with different $V_{bias}$. The EDS images in Figure 3a show that the deposited nanoparticle at $V_{bias}$ = −0.1 V is indeed enriched in Cu (∼99% mole fraction based on EDS). The mole fraction of Cu decreases further as $V_{bias}$ increases, reaching 76% at 0 V (Figure 3b) and 48% at 0.05 V (Figure 3c). At $V_{bias}$ = 0.2 V, the mole fraction of Cu in the particle decreases to 7%, while the mole fraction of Ag reaches 93%. The morphology of the particles suggests an

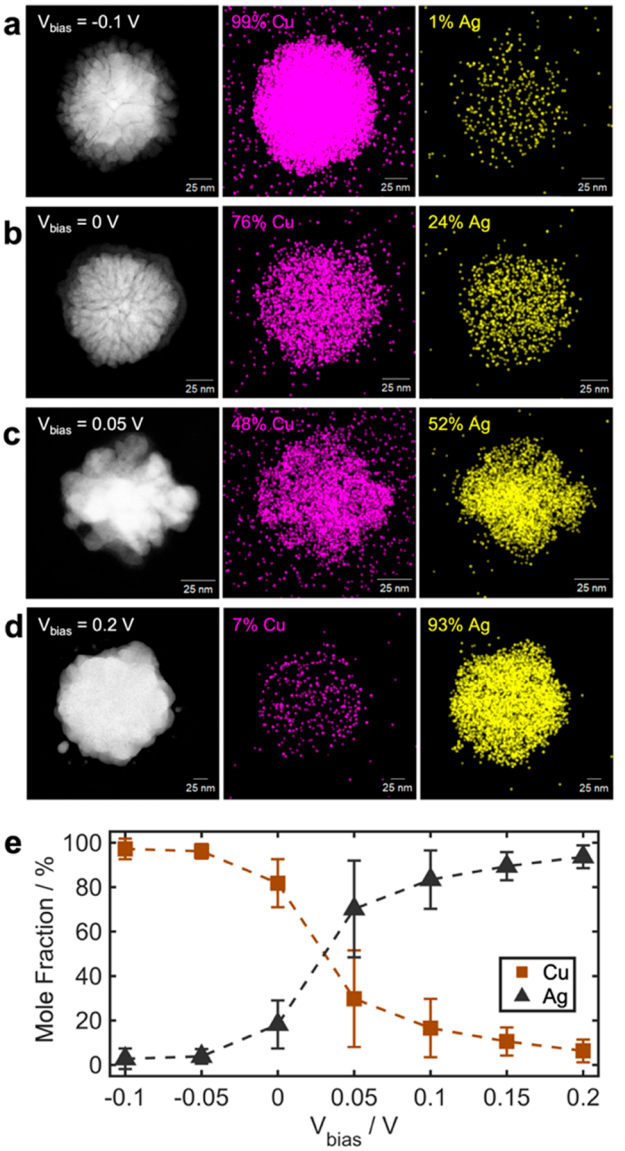


**Figure 3. Annular dark field-scanning transmission electron microscopy (ADF-STEM) images and energy-dispersive X-ray spectroscopy (EDS) elemental maps of Cu–Ag nanoparticles fabricated at $V_{WE}$ = −0.7 V for 0.2 s by SECCM. (a–d) STEM images and EDS maps of Cu–Ag nanoparticles with continuously varying composition: (a) 99% Cu, 1% Ag; (b) 76% Cu, 24% Ag; (c) 48% Cu, 52% Ag; (d) 7% Cu, 93% Ag. (e) Mole fraction of Cu–Ag nanoparticles obtained from EDS analysis as a function of $V_{bias}$. Error bars represent the standard deviation from $n$ = 10.**



https://doi.org/10.1021/acsnano.3c06011
ACS Nano 2023, 17, 22499–22507

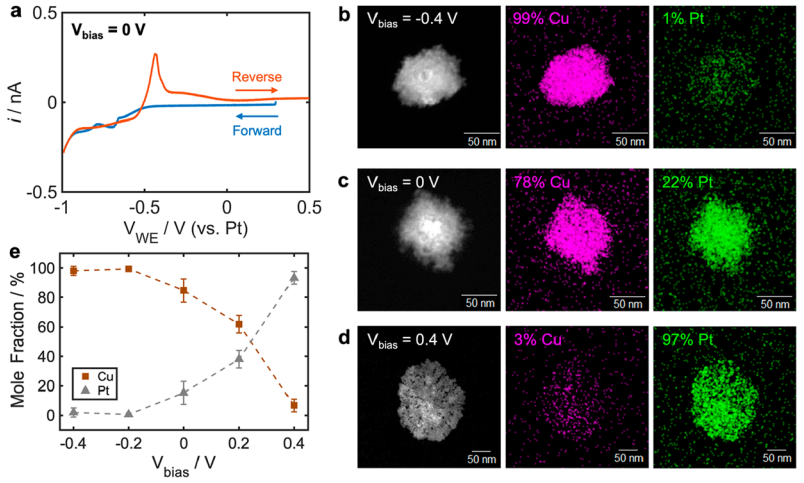


**Figure 4. Synthesis of Cu−Pt bimetallic particles. (a) Cyclic voltammogram of Cu−Pt by SECCM. The left barrel contains 2 mM $Cu(ClO_4)_2$ + 2 mM $HClO_4$, and the right barrel contains 2 mM $H_2PtCl_6$ + 2 mM $HClO_4$. Scan rate: 0.5 V/s. (b−d) SEM images and EDS elemental maps of Cu−Pt nanoparticles synthesized at $V_{WE}$ = −0.8 V for 0.2 s, showing (b) 99% Cu and 1% Pt at $V_{bias}$ = −0.4 V, (c) 78% Cu and 22% Pt at $V_{bias}$ = 0 V, and (d) 3% Cu and 97% Pt at $V_{bias}$ = +0.4 V. (e) Mole fraction of Cu−Pt nanoparticles observed by EDS. Error bars indicate the standard deviation from $n$ = 10.**

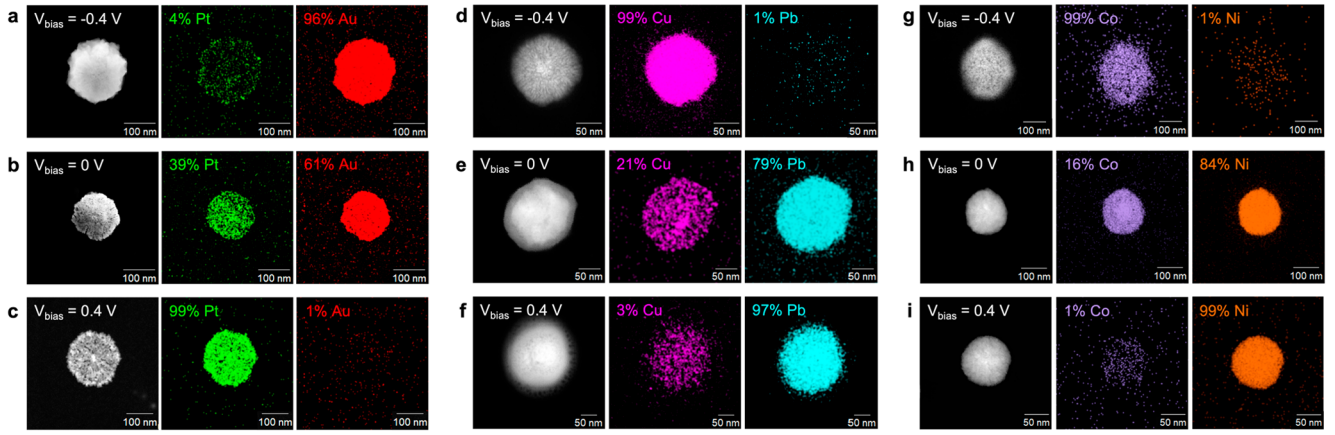


**Figure 5. Synthesis of various bimetallic particles by SECCM. (a−c) TEM images and elemental maps of Au−Pt nanoparticles synthesized at $V_{WE}$ = −0.8 V showing different compositions at different $V_{bias}$. 2 mM $H_2PtCl_6$ + 2 mM $HClO_4$ for Pt and 2 mM $HAuCl_4$ + 2 mM $HClO_4$ for Au were used. (d−f) TEM images and EDS elemental maps of Cu−Pb nanoparticles synthesized at $V_{WE}$ = −1.2 V at different $V_{bias}$. Two mM $Cu(ClO_4)_2$ + 2 mM $HClO_4$ for Cu and 2 mM $Pb(ClO_4)_2$ + 2 mM $HClO_4$ for Pb were used. (g−i) TEM images and EDS elemental maps of Co−Ni nanoparticles synthesized at $V_{WE}$ = −1.25 V at different $V_{bias}$. 2 mM $CoCl_2$ + 2 mM $HClO_4$ for Co and 2 mM $NiCl_2$ + 2 mM $HClO_4$ for Ni were used. Deposition time: 0.3 s.**

aggregative growth mechanism during the deposition. However, the composition and the spatial distribution of each element are uniform in the particles regardless of the deposition conditions and the final particle morphology, suggesting the formation of Cu−Ag alloy (see Section S6 in the Supporting Information). The tuning of the mole fractions of Ag and Cu in the nanoparticle by $V_{bias}$ is summarized in Figure 3e. The size of the particle can also be tuned by the deposition time (Figure S10).

To deposit alloy particles, the potential needs to be more negative than the equilibrium potential of the most inert metal component (e.g., Cu in the Cu−Ag system). This can create challenges in controlling the rate of nucleation and therefore the ability to ensure single-particle deposition. The choice of working electrode potential can also be used to tune the composition of the deposition as shown in Figure S11.

Overall, the EDS images in Figure 3 show that Cu and Ag are homogeneously mixed. Note that thermal methods have been used to synthesize Cu−Ag bimetallic particles but often result in phase segregation as predicted by equilibrium.[10] Our method shows a homogeneous mixing of Cu and Ag elements in each particle (see analysis in Figure S12), highlighting one of the capabilities of synthesizing nonequilibrium alloy particles via electrochemical methods due to facile control of the driving force via electrode potential.

We further demonstrate the generality of the method to control the composition by electrodeposition of Cu−Pt particles with various compositions, which have shown to be good catalyst candidates for methanol oxidation reactions.[34] The right barrel of the dual-barrel pipet is replaced with 2 mM $H_2PtCl_6$ in 2 mM $HClO_4$, while the left barrel remains the same $Cu^{2+}$ solution (2 mM). Figure 4a shows an SECCM voltammogram for the deposition at $V_{bias}$ = 0 V. In the


https://doi.org/10.1021/acsnano.3c06011
ACS Nano 2023, 17, 22499−22507

negative-going scan, multiple cathodic voltammetric waves are observed when $V_{WE}$ is lower than −0.5 V, corresponding to the reduction of Pt and Cu. Peak assignment based on bulk voltammetric experiments on glassy-carbon electrodes is discussed in Section S3 in the Supporting Information and Figure S7. Figure 4b–d shows the SEM images of the deposited particles and the corresponding EDS maps, which show that the fraction of Pt increases and that of Cu decreases as $V_{bias}$ increases. At negative $V_{bias}$, e.g., −0.4 V, the particle is enriched with Cu (Figure 4b). At positive $V_{bias}$, e.g., 0.4 V, the particle is enriched with Pt (Figure 4d). Alloy particles containing significant amounts of Cu and Pt can be deposited at intermediate $V_{bias}$, e.g., 0 V. The mole fraction of Cu and Pt in the particles estimated from EDS as a function of $V_{bias}$ is summarized in Figure 4e.

The versatility of the method in depositing bimetallic nanoparticles is further showcased through different elemental combinations by changing the metal precursor solutions. As shown in Figure 5, Au–Pt, Cu–Pb, and Co–Ni were deposited, and the elemental maps show a homogeneous mixing of each element in the nanoparticle. In addition, the elemental composition in the particles can be tuned by $V_{bias}$ under the same principle of fluidic control as that demonstrated for Cu–Ag (Figure 3) and Cu–Pt (Figure 4).

Moreover, we substantiate our ability to control the spatial distribution of the particles and the elemental composition in each particle by creating a pattern of a Longhorn from deposited particles. The minimum deposition separation distance is experimentally determined to be ∼1 μm when a 340 nm radius pipet was used (Figure S13). As can be seen in the SEM image (Figure 6a), the nanoparticles are faithfully

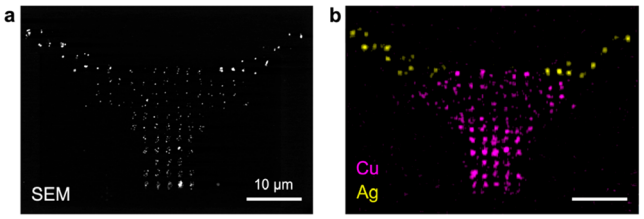


**Figure 6. Multielement electrodeposition for surface patterning. (a) SEM image and (b) EDS map of Cu-rich or Ag-rich nanoparticles fabricated on the substrate by one dual-channel pipet (scale bar: 10 μm).**

deposited, and the 150 pixels form an image of a Longhorn. Each pixel contains nanoparticles of ∼100 nm in radius. The EDS mapping also demonstrates that we can control the composition at each pixel (Figure 6b). The horns of the Longhorn were purposely decorated by particles enriched with Ag using the same nanopipet. The ability to deposit multielements using the same pipet allows precision fabrication of the nanoparticle architecture, which is potentially useful in additive manufacturing and fabrication of architecture for cascade catalysis.[35,36]

Lastly, we demonstrate that alloy particle arrays synthesized in this manner can be directly used for the screening of the electrocatalytic activity. Cu–Ag is chosen to screen for their electrocatalytic activity in the hydrogen evolution reaction (HER) because it are less expensive than Pt, yet it is of high interest for electrochemical $CO_2$ reduction where the HER is the most important competing reaction.[37] Five different compositions of Cu–Ag nanoparticle alloys were synthesized via different bias potentials ranging from −0.2 to 0.2 V, as depicted in Figure 7a. The fraction of Cu in the Cu–Ag

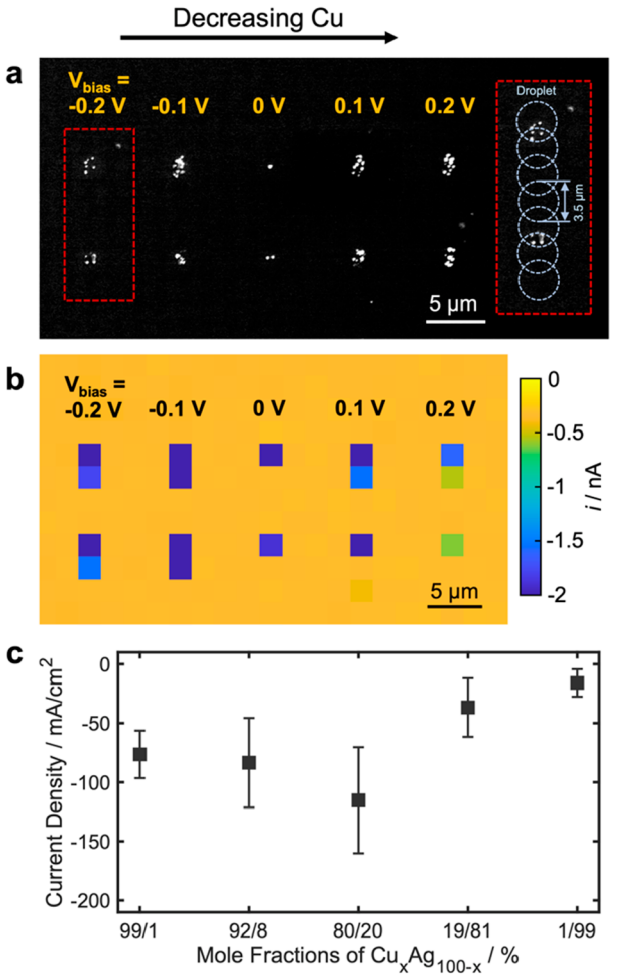


**Figure 7. Local electrochemical mapping was used to screen the electrocatalytic activity of fabricated nanoparticles via SECCM. (a) SEM image of the Cu–Ag nanoparticle array synthesized with different $V_{bias}$. The inset image depicts the location of droplets during electrochemical mapping. (b) Current heat map at −1.161 V vs standard hydrogen electrode (SHE) of the Cu–Ag particle array shown in (a). (c) Current density of Cu–Ag nanoparticles as a function of mole fractions, corresponding to the applied bias potential ranging from −0.2 to 0.2 V. Error bars represent the standard deviation from triplicates.**

nanoparticles decreases from left to right, while the particles in the same column were deposited under the same conditions and shared similar compositions. An ∼3 μm diameter single-barrel pipet containing 50 mM $HClO_4$ was used as an SECCM probe to voltammetrically screen the activity of the HER. A hopping voltammetric scan mode was used with a 2 μm stepping distance. The local voltammograms are visualized by plotting the current at −1.161 V vs the standard hydrogen electrode (SHE) as a heat map, as shown in Figure 7b. Each pixel in the map corresponds to a single local voltammetric measurement, and the local current was higher at the nanoparticles compared to that on the GC substrate. To validate the composition–activity correlation of Cu–Ag nanoparticles, the composition is determined by EDS, while the current is normalized to the current density using the


https://doi.org/10.1021/acsnano.3c06011
ACS Nano 2023, 17, 22499–22507

surface area of the particles determined by atomic force microscopy (see Figures S14 and S15 for the measurement). As shown in Figure 7c, the HER current density on the Cu−Ag nanoparticles first increases and then decreases as the mole fraction of Cu decreases, and the maximum activity is reached with nanoparticles containing 80% Cu and 20% Ag. Furthermore, Cu-rich nanoparticles exhibited HER activity higher than that of Ag-rich particles.

## CONCLUSION

In summary, we have developed a dual-channel nanopipet method that enables precise synthesis of bimetallic nanoparticle libraries of countinous variation in composition. Nanofluidic control by the voltage bias in the dual-channel nanopipet allows precise control of the electrodeposition rate of each element, creating bimetallic nanoparticles with precise composition. The control of composition is demonstrated by various bimetallic nanoparticles, including Cu−Ag, Cu−Pt, Au−Pt, Cu−Pb, and Co−Ni. On-demand nanoparticle alloy synthesis is further demonstrated by surface patterning from nanoparticles, where the composition can be controlled at the single-pixel level. We further demonstrated that the synthesized bimetallic nanoparticle arrays with varying compositions are suitable for screening the electrocatalytic activity via SECCM. The ability to synthesize libraries of nanoparticle arrays with gradient compositions is important for the accelerated discovery of materials in electrocatalysis and beyond. While the method is demonstrated using dual-barrel pipets for the electrodeposition of bimetallic nanoparticles, the same concept of in situ composition control can be further extended to include multiple elements, which will be reported in a separate study, by increasing the number of barrels, potentially enabling the high-throughput synthesis of a library of high-entropy alloys with different compositions. The ability of submicrometer and nanoscale patterning can further benefit the development of nanoscale additive manufacturing, as well as creating architectures for tandem catalysis.

## METHODS

**Chemical and Materials.** Copper (Cu), silver (Ag), platinum (Pt), lead (Pb), gold (Au), cobalt (Co), and nickel (Ni) solutions were prepared with copper(II) perchlorate hexahydrate (Sigma-Aldrich), silver perchlorate hydrate (Sigma-Aldrich), chloroplatinic acid hydrate (Sigma-Aldrich), lead(II) perchlorate hydrate (Sigma-Aldrich), gold(III) chloride hydrate (Sigma-Aldrich), cobalt(II) chloride hexahydrate (Thermo Scientific), nickel(II) chloride hexahydrate (Sigma-Aldrich), perchloric acid (70%, Alfa Aesar), and deionized water (18.2 MΩ cm, Synergy Water Purification System). Platinum wires (0.1 mm diameter, 99.9% metals basis, Alfa Aesar) and palladium wires (0.5 mm diameter, 99.9% metals basis, Fisher Scientific) were used as quasireference counter electrodes (QRCE) in SECCM.

**Pipet Preparation.** Dual channel nanopipets were fabricated from theta quartz capillaries (QT120-90-7.5, Sutter Instrument) using the P-2000 micropipet puller (Sutter Instrument). The pulling parameters were HEAT = 750, FIL = 4, VEL = 40, DEL = 130, and PUL = 30 for line 1 and HEAT = 640, FIL = 3, VEL = 30, DEL = 130, and PUL = 100 for line 2.

**SECCM Measurements.** The SECCM experiment was performed on a home-built scanning electrochemical probe system. The vertical movement of the pipet was controlled by a one-axis piezo-positioner (P-621.1CD, Physik Instrumente), and the $x$−$y$ direction of the substrate was controlled by a two-axis piezo positioner (NPXY300, nPoint). The scanning probe system was mounted on a mechanical vibration isolator (Minus K Technology, BM-4) and enclosed in a custom-built Faraday cage. Patch-clamp amplifiers (Dagan Chem-clamp) were used for voltage control and current measurement. The data acquisition and instrument control were performed by using an FPGA card (PCIe-7846, National Instrument) and interfaced with the Warwick Electrochemical-Scanning Probe Microscopy Platform (WEC-SPM) software, which was kindly provided by the Warwick Electrochemistry & Interfaces Group (WEIG).[29]

**Energy Dispersive Spectroscopy (EDS).** Annular dark field-scanning transmission electron microscopy (ADF-STEM) was performed by using a JEOL NEOARM instrument equipped with a probe corrector for STEM operated at an accelerating voltage of 200 kV and an average beam current of 10 μA. A dwell time of 10 μs was used for imaging. EDS was conducted in a JEOL NEOARM instrument equipped with a JEOL large-angle silicon drift detector (0.96 sr). Scanning electron microscopy (SEM) was performed by using a Scios2 Dual Beam SEM at an accelerating voltage of 10 kV and a current of 13 nA. For each spectrum image, at least 50 frames were collected so that sufficient counts were recorded. Map processing was performed with the ThermoFisher Pathfinder software. The TEM and SEM images were further analyzed by using ImageJ.

**Bulk Electrochemistry.** All of the bulk electrochemistry was performed using a potentiostat (CH760, CH Instruments) in a three-electrode system with glassy carbon (GC) as a working electrode. Prior to each experiment, the GC electrode was polished with an alumina particle slurry with a decreasing size from 0.3 to 0.05 μm. After polishing, the GC electrode was thoroughly rinsed with deionized water and dried under nitrogen gas.

## ASSOCIATED CONTENT

### Supporting Information

The Supporting Information is available free of charge at https://pubs.acs.org/doi/10.1021/acsnano.3c06011.

Extended experimental results, characterization of nanopipets, finite element simulation, assignment of the stripping peaks, cyclic voltammograms using Pd−$H_2$ electrodes, nanoparticle deposition under constant potential, composition analysis of fabricated bimetallic nanoparticles, spatial control of the nanoparticle deposition, and AFM analysis of deposited bimetallic nanoparticles (PDF)

## AUTHOR INFORMATION


### Corresponding Author

**Hang Ren** − *Department of Chemistry, The University of Texas at Austin, Austin, Texas 78712, United States;* orcid.org/0000-0002-9480-8881; Email: hren@utexas.edu

### Authors

**Heekwon Lee** − *Department of Chemistry, The University of Texas at Austin, Austin, Texas 78712, United States*

**Kevin C. Matthews** − *Walker Department of Mechanical Engineering and Texas Materials Institute, The University of Texas at Austin, Austin, Texas 78712, United States;* orcid.org/0000-0002-4995-2489

**Xun Zhan** − *Texas Materials Institute, The University of Texas at Austin, Austin, Texas 78712, United States*

**Jamie H. Warner** − *Walker Department of Mechanical Engineering and Texas Materials Institute, The University of Texas at Austin, Austin, Texas 78712, United States;* orcid.org/0000-0002-1271-2019

Complete contact information is available at: https://pubs.acs.org/10.1021/acsnano.3c06011

## Notes

The authors declare no competing financial interest.

## ACKNOWLEDGMENTS

H.R. and H.L. acknowledge the support from the Chemical Measurement & Imaging Program (CMI) at the National Science Foundation under Grant No. CHE-2240113 and the Welch Foundation under F-2158-2023040. We also acknowledge the use of the facility at the Texas Materials Institute, the Center for Electrochemistry, and the Instrument Design and Repair at UT Austin. We thank Prof. Kim McKelvey for the software support for WEC-SPM.

## REFERENCES

(1) Talapin, D. V.; Shevchenko, E. V. Introduction: Nanoparticle Chemistry. *Chem. Rev.* **2016**, *116*, 10343−10345.
(2) You, H.; Yang, S.; Ding, B.; Yang, H. Synthesis of Colloidal Metal and Metal Alloy Nanoparticles for Electrochemical Energy Applications. *Chem. Soc. Rev.* **2013**, *42*, 2880−2904.
(3) Swisher, J. H.; Jibril, L.; Petrosko, S. H.; Mirkin, C. A. Nanoreactors for Particle Synthesis. *Nat. Rev. Mater.* **2022**, *7*, 428−448.
(4) Koo, W.-T.; Millstone, J. E.; Weiss, P. S.; Kim, I.-D. The Design and Science of Polyelemental Nanoparticles. *ACS Nano* **2020**, *14*, 6407−6413.
(5) Park, J. H.; Ahn, H. S. Electrochemical Synthesis of Multimetallic Nanoparticles and Their Application in Alkaline Oxygen Reduction Catalysis. *Appl. Surf. Sci.* **2020**, *504*, 144517.
(6) Li, J.; Sun, S. Intermetallic Nanoparticles: Synthetic Control and Their Enhanced Electrocatalysis. *Acc. Chem. Res.* **2019**, *52*, 2015−2025.
(7) Li, Z.; Wang, S.; Chin, W. S.; Achenie, L. E.; Xin, H. High-Throughput Screening of Bimetallic Catalysts Enabled by Machine Learning. *J. Mater. Chem. A* **2017**, *5*, 24131−24138.
(8) Toshima, N.; Yonezawa, T. Bimetallic Nanoparticles—Novel Materials for Chemical and Physical Applications. *New J. Chem.* **1998**, *22*, 1179−1201.
(9) Glasscott, M. W.; Pendergast, A. D.; Goines, S.; Bishop, A. R.; Hoang, A. T.; Renault, C.; Dick, J. E. Electrosynthesis of High-Entropy Metallic Glass Nanoparticles for Designer, Multi-Functional Electrocatalysis. *Nat. Commun.* **2019**, *10*, 2650.
(10) Chen, P.-C.; Liu, M.; Du, J. S.; Meckes, B.; Wang, S.; Lin, H.; Dravid, V. P.; Wolverton, C.; Mirkin, C. A. Interface and Heterostructure Design in Polyelemental Nanoparticles. *Science* **2019**, *363*, 959−964.
(11) Xu, Z.; Lai, E.; Shao-Horn, Y.; Hamad-Schifferli, K. Compositional Dependence of the Stability of AuCu Alloy Nanoparticles. *Chem. Commun.* **2012**, *48*, 5626−5628.
(12) Xu, X.; Valavanis, D.; Ciocci, P.; Confederat, S.; Marcuccio, F.; Lemineur, J.-F.; Actis, P.; Kanoufi, F.; Unwin, P. R. The New Era of High-Throughput Nanoelectrochemistry. *Anal. Chem.* **2023**, *95*, 319−356.
(13) Gurau, B.; Viswanathan, R.; Liu, R.; Lafrenz, T. J.; Ley, K. L.; Smotkin, E. S.; Reddington, E.; Sapienza, A.; Chan, B. C.; Mallouk, T. E.; et al. Structural and Electrochemical Characterization of Binary, Ternary, and Quaternary Platinum Alloy Catalysts for Methanol Electro-Oxidation. *J. Physic. Chem. B* **1998**, *102*, 9997−10003.
(14) Hitt, J. L.; Li, Y. C.; Tao, S.; Yan, Z.; Gao, Y.; Billinge, S. J. L.; Mallouk, T. E. A High Throughput Optical Method for Studying Compositional Effects in Electrocatalysts for $CO_2$ Reduction. *Nat. Commun.* **2021**, *12*, 1114.
(15) Chen, P.-C.; Liu, X.; Hedrick, J. L.; Xie, Z.; Wang, S.; Lin, Q.-Y.; Hersam, M. C.; Dravid, V. P.; Mirkin, C. A. Polyelemental Nanoparticle Libraries. *Science* **2016**, *352*, 1565−1569.
(16) Kluender, E. J.; Hedrick, J. L.; Brown, K. A.; Rao, R.; Meckes, B.; Du, J. S.; Moreau, L. M.; Maruyama, B.; Mirkin, C. A. Catalyst Discovery through Megalibraries of Nanomaterials. *Proc. Natl. Acad. Sci. U.S.A.* **2019**, *116*, 40−45.
(17) Chen, P.-C.; Liu, G.; Zhou, Y.; Brown, K. A.; Chernyak, N.; Hedrick, J. L.; He, S.; Xie, Z.; Lin, Q.-Y.; Dravid, V. P.; O'Neill-Slawecki, S. A.; Mirkin, C. A. Tip-Directed Synthesis of Multimetallic Nanoparticles. *J. Am. Chem. Soc.* **2015**, *137*, 9167−9173.
(18) König, D.; Richter, K.; Siegel, A.; Mudring, A. V.; Ludwig, A. High-Throughput Fabrication of Au-Cu Nanoparticle Libraries by Combinatorial Sputtering in Ionic Liquids. *Adv. Funct. Mater.* **2014**, *24*, 2049−2056.
(19) Senkan, S.; Kahn, M.; Duan, S.; Ly, A.; Leidholm, C. High-Throughput Metal Nanoparticle Catalysis by Pulsed Laser Ablation. *Catal. Today* **2006**, *117*, 291−296.
(20) Bek, A.; Jansen, R.; Ringler, M.; Mayilo, S.; Klar, T. A.; Feldmann, J. Fluorescence Enhancement in Hot Spots of AFM-Designed Gold Nanoparticle Sandwiches. *Nano Lett.* **2008**, *8*, 485−490.
(21) Toh, H. S.; Jurkschat, K.; Compton, R. G. The Influence of the Capping Agent on the Oxidation of Silver Nanoparticles: Nano-Impacts versus Stripping Voltammetry. *Eur. J. Chem.* **2015**, *21*, 2998−3004.
(22) Tarolla, N. E.; Voci, S.; Reyes-Morales, J.; Pendergast, A. D.; Dick, J. E. Electrodeposition of Ligand-Free Copper Nanoparticles from Aqueous Nanodroplets. *J. Mater. Chem. A* **2021**, *9*, 20048−20057.
(23) Kleijn, S. E. F.; Lai, S. C. S.; Koper, M. T. M.; Unwin, P. R. Electrochemistry of Nanoparticles. *Angew. Chem., Int. Ed.* **2014**, *53*, 3558−3586.
(24) Yamauchi, Y.; Tonegawa, A.; Komatsu, M.; Wang, H.; Wang, L.; Nemoto, Y.; Suzuki, N.; Kuroda, K. Electrochemical Synthesis of Mesoporous Pt-Au Binary Alloys with Tunable Compositions for Enhancement of Electrochemical Performance. *J. Am. Chem. Soc.* **2012**, *134*, 5100−5109.
(25) Jin, Z.; Li, P.; Fang, Z.; Yu, G. Emerging Electrochemical Techniques for Probing Site Behavior in Single-Atom Electrocatalysts. *Acc. Chem. Res.* **2022**, *55*, 759−769.
(26) Ebejer, N.; Güell, A. G.; Lai, S. C. S.; McKelvey, K.; Snowden, M. E.; Unwin, P. R. Scanning Electrochemical Cell Microscopy: A Versatile Technique for Nanoscale Electrochemistry and Functional Imaging. *Annu. Rev. Anal. Chem.* **2013**, *6*, 329−351.
(27) Rahman, M. M.; Tolbert, C. L.; Saha, P.; Halpern, J. M.; Hill, C. M. On-Demand Electrochemical Fabrication of Ordered Nanoparticle Arrays using Scanning Electrochemical Cell Microscopy. *ACS Nano* **2022**, *16*, 21275−21282.
(28) Ciocci, P.; Valavanis, D.; Meloni, G. N.; Lemineur, J. F.; Unwin, P. R.; Kanoufi, F. Optical Super-Localisation of Single Nanoparticle Nucleation and Growth in Nanodroplets. *ChemElectroChem.* **2023**, *10*, No. e202201162.
(29) Snowden, M. E.; Güell, A. G.; Lai, S. C. S.; McKelvey, K.; Ebejer, N.; O'Connell, M. A.; Colburn, A. W.; Unwin, P. R. Scanning Electrochemical Cell Microscopy: Theory and Experiment for Quantitative High Resolution Spatially-Resolved Voltammetry and Simultaneous Ion-Conductance Measurements. *Anal. Chem.* **2012**, *84*, 2483−2491.
(30) Wang, Y.; Gordon, E.; Ren, H. Mapping the Nucleation of $H_2$ Bubbles on Polycrystalline Pt via Scanning Electrochemical Cell Microscopy. *J. Phys. Chem. Lett.* **2019**, *10*, 3887−3892.
(31) Wahab, O. J.; Kang, M.; Daviddi, E.; Walker, M.; Unwin, P. R. Screening Surface Structure-Electrochemical Activity Relationships of Copper Electrodes under $CO_2$ Electroreduction Conditions. *ACS Catal.* **2022**, *12*, 6578−6588.
(32) Ornelas, I. M.; Unwin, P. R.; Bentley, C. L. High-Throughput Correlative Electrochemistry-Microscopy at a Transmission Electron Microscopy Grid Electrode. *Anal. Chem.* **2019**, *91*, 14854−14859.
(33) Blount, B.; Juarez, G.; Wang, Y.; Ren, H. iR Drop in Scanning Electrochemical Cell Microscopy. *Faraday Discuss.* **2022**, *233*, 149−162.
(34) Du, X.; Luo, S.; Du, H.; Tang, M.; Huang, X.; Shen, P. K. Monodisperse and Self-Assembled Pt-Cu Nanoparticles as an Efficient

Electrocatalyst for the Methanol Oxidation Reaction. *J. Mater. Chem. A* **2016**, *4*, 1579−1585.
(35) Wang, L.; Wang, L.; Meng, X.; Xiao, F. S. New Strategies for the Preparation of Sinter-Resistant Metal-Nanoparticle-Based Catalysts. *Adv. Mater.* **2019**, *31*, 1901905.
(36) Qian, D.; Zhang, J. Yne-Enones Enable Diversity-Oriented Catalytic Cascade Reactions: A Rapid Assembly of Complexity. *Acc. Chem. Res.* **2020**, *53*, 2358−2371.
(37) Koolen, C. D.; Oveisi, E.; Zhang, J.; Li, M.; Safonova, O. V.; Pedersen, J. K.; Rossmeisl, J.; Luo, W.; Züttel, A. Low-Temperature Non-Equilibrium Synthesis of Anisotropic Multimetallic Nanosurface Alloys for Electrochemical $CO_2$ Reduction. *Nat. Synth.* **2023**, DOI: 10.1038/s44160-023-00387-3.



https://doi.org/10.1021/acsnano.3c06011
*ACS Nano* 2023, 17, 22499−22507